



Identification of Pyrazole Derivatives of Usnic Acid as Novel Inhibitor of SARS-CoV-2 Main Protease Through Virtual Screening Approaches

Miah Roney^{1,2} · Gagandeep Singh^{3,4} · A. K. M. Moyeenul Huq^{2,5} · Md Shaekh Forid⁶ · Wan Maznah Binti Wan Ishak⁶ · Kamal Rullah⁷ · Mohd Fadhilzil Fasihi Mohd Aluwi^{1,2} · Saiful Nizam Tajuddin^{1,2}

Received: 30 August 2022 / Accepted: 12 January 2023 / Published online: 8 February 2023
© The Author(s), under exclusive licence to Springer Science+Business Media, LLC, part of Springer Nature 2023

Abstract

The infection produced by the SARS-CoV-2 virus remains a significant health crisis worldwide. The lack of specific medications for COVID-19 necessitates a concerted effort to find the much-desired therapies for this condition. The main protease (M^{pro}) of SARS-CoV-2 is a promising target, vital for virus replication and transcription. In this study, fifty pyrazole derivatives were tested for their pharmacokinetics and drugability, resulting in eight hit compounds. Subsequent molecular docking simulations on SARS-CoV-2 main protease afforded two lead compounds with strong affinity at the active site. Additionally, the molecular dynamics (MD) simulations of lead compounds (17 and 39), along with binding free energy calculations, were accomplished to validate the stability of the docked complexes and the binding poses achieved in docking experiments. Based on these findings, compound 17 and 39, with their favorable projected pharmacokinetics and pharmacological characteristics, are the proposed potential antiviral candidates which require further investigation to be used as anti-SARS-CoV-2 medication.

Keywords SARS-CoV-2 · Pyrazole derivatives of Usnic acid · ADMET · Drug-likeness · Docking · Molecular dynamics simulation

Introduction

Viral respiratory infections in humans are mainly caused by Coronaviruses (CoVs). The SARS coronavirus (SARS-CoV) and MERS-CoVs are the most virulent types transmitted to humans from animals and could lead to mild to severe respiratory infections. These two sparked global epidemics during the last twenty years, with very high mortality rates

in 2003 and 2012 [1]. In December 2019, swiftly dispersing cases of pneumonia disease were discovered in Wuhan city of China [2], which was caused by a novel coronavirus strain that was identified later. This strain has an 82% similar positive-stranded RNA genome to that of the SARS-CoV, a clade of the beta-coronavirus, named SARS-CoV-2 [3, 4]. A big replicase gene encompassing non-structural proteins is found in the genome, followed by structural and auxiliary genes [5]. Both polyprotein 1a and polyprotein 1b (pp1a and pp1b), which are eventually transformed into mature

Miah Roney and Gagandeep Singh have authors contributed equally.

✉ A. K. M. Moyeenul Huq
moyeenul@ump.edu.my

✉ Mohd Fadhilzil Fasihi Mohd Aluwi
fasihi@ump.edu.my

¹ Faculty of Industrial Sciences and Technology, Universiti Malaysia Pahang, Lebuhraya Tun Razak, 26300 Gambang, Kuantan, Pahang Darul Makmur, Malaysia

² Bio Aromatic Research Centre, Universiti Malaysia Pahang, Lebuhraya Tun Razak, 26300 Gambang, Kuantan, Pahang Darul Makmur, Malaysia

³ Section of Microbiology, Central Ayurveda Research Institute, Jhansi, Uttar Pradesh, India

⁴ Kusuma School of Biological Sciences, Indian Institute of Technology, Delhi, India

⁵ School of Medicine, Department of Pharmacy, University of Asia Pacific, 74/A, Green Road, Dhaka 1205, Bangladesh

⁶ Faculty of Chemical and Processing Engineering Technology, Universiti Malaysia Pahang, Lebuhraya Tun Razak, 26300 Gambang, Kuantan, Pahang Darul Makmur, Malaysia

⁷ Kulliyah of Pharmacy, International Islamic University Malaysia (IIUM), Jalan Sultan Ahmad Shah, 25200 Kuantan, Pahang, Malaysia

non-structural proteins by main protease (M^{pro}) and papain-like proteases, are encoded by the first of the two open reading frames (ORFs) of the replicase gene. These enzymes are essential for viral replication and transcription [6, 7]. SARS-CoV-2 possesses a large number of structural and non-structural proteins. The crystal structure of the M^{pro} or chymotrypsin-like protease ($3CL^{pro}$) from SARS-CoV-2 was successfully constructed by Liu et al. [8]. The M^{pro} protein is also crucial for viral proteolytic maturation. Thus, M^{pro} could be a potential and effective therapeutic target for the novel coronavirus disease by inhibiting the polypeptide cleavage of SARS-CoV-2.

The World Health Organization (WHO) formally called the disease COVID-19 on February 11th, 2020 [9], and essentially declared a pandemic on March 11th, 2020, as the virus spread exponentially over the globe [10]. According to the situation report, there are 509,854,571 cumulative confirmed cases worldwide, with 6,244,664 deaths as of April 26th, 2022 [11]. Pfizer's antiviral Paxlovid, a protease inhibitor, got the emergency US Food and Drug Administration (FDA) approval to administer to COVID-19 patients on December 22nd, 2021. However, its associated drug–drug interactions may limit its use in the community [12]. Furthermore, a few vaccines are on the market to combat this lethal viral infection. Some studies support using traditional medicines as alternative and adjuvant therapies in SARS-CoV-2 disease. So, continuous efforts are still ongoing to integrate western medications and traditional medicines for devising proper therapeutic strategies [13]. Antiviral therapies have been demonstrated to be effective against viral enzymes. As a result, most antiviral drugs have been used for SARS-CoV-2 treatment at the start of a diagnosis [14]. Since January 2020, numerous clinical trials have been conducted on antiviral, anti-inflammatory, and antimalarial medications for managing COVID-19 disease [15, 16].

The best source of therapeutic compounds is natural products with anticancer [17, 18], antiviral [19], antibacterial [18], antioxidant [20], and anti-inflammatory [21] properties, as well as anti-herbivorous activity [22]. Lichens have traditionally been utilized for various illnesses in many cultures and are a potential source of novel antiviral agents [23, 24]. A lichen-derived secondary metabolite Usnic acid (UA), shows a unique range of bioactivity, including activity against several gram-positive bacteria such as *Staphylococcus epidermidis*, *Staphylococcus aureus*, *Enterococcus faecalis*, *Mycobacterium tuberculosis*, and several pathogenic fungi. When used in polyurethanes or bone cement, it has recently been proven to suppress biofilm formation by *Staphylococcus* spp. [25, 26]. As a result, this molecule is thus being investigated as a potential agent to be adsorbed onto the surface of medical devices as a substitute for conventional antibiotics to prevent bacterial infections caused by medical equipment. Furthermore, this compound has

anti-parasitic [27], anti-inflammatory [28], antiviral [29], anti-nociceptive, anti-mycotic [27], and anesthetic [30] activities. The anti-tumor action of UA was initially discovered in mice with lung cancer and P388 leukemia [31]. Furthermore, based on the docking result by Prateeksha et al. [32] which exhibited the ability of UA to inhibit the interaction between the viral receptor binding domain (RBD) of trimeric spike glycoprotein (SGP) with the host angiotensin-converting enzyme-2 (ACE-2) [32] suggests its therapeutic potentiality against SARS-CoV-2.

Thus, the research objective was to use *in-silico* techniques to find novel pyrazole derivatives of UA as potential anti-SARS-CoV-2 lead compounds. A total of 50 pyrazole derivatives of UA (Table S1) were initially obtained from the literature. Following that, drug-likeness and ADMET screening was performed, and eight compounds were chosen based on their pharmacokinetic features. These were then subjected to molecular docking against SARS-CoV-2 main protease (M^{pro}), which yielded two lead compounds (Table 1) compared to the reference compound (Co-crystallized ligand, 11a). The resultant compounds were further subjected to molecular dynamics (MD) simulation to estimate the docking accuracy and binding stability.

Methodology

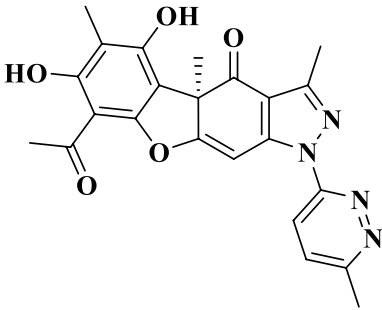
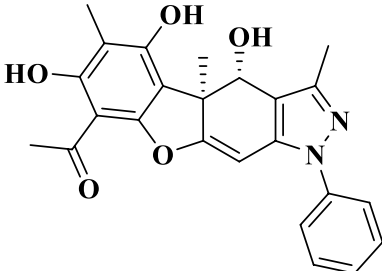
Drug-Like Properties and ADMET Study

Several predictors were used to characterize the side effects and potency of the selected ligands (Table S1) as drugs, including Lipinski's rule of five (Molecular weight, LogP, Hydrogen bond acceptor and donor, and Topological polar surface area) and ADMET properties (Aqueous solubility, Human intestine absorption, Blood–brain barrier, CYP substrate inhibitor, hERG inhibitor, and hepatotoxicity). The online tool pkCSM (<http://biosig.unimelb.edu.au/pkcsml/>) was used to evaluate the pharmacokinetic variables [33] of both ligands and standard (Co-crystallized ligand, 11a) molecules.

Structure-Based Screening

The crystal structure of SARS-CoV-2 M^{pro} with the PDB code 6LZE was used as the target protein for docking [34, 35]. The CB-Dock (Cavity-detection guided Blind Docking) tool was used for protein–ligand docking [36, 37] of eight pyrazole derivatives of UA (obtained from drug-likeness and ADMET screening) with the M^{pro} target. These ligands were acquired from several literature sources, generated with the ChemSketch tool, and saved in.mol format. The CB-Dock protein–ligand docking tool quickly locates the binding region, calculates the center's size and location,

Table 1 Structure, IUPAC name, chemical formula, and molecular weight of newly discovered small-molecule inhibitors (17 and 39)

Compound number	Molecular structure	IUPAC name	Chemical formula	Molecular weight (g/mol)
17		(R)-8-acetyl-5,7-dihydroxy-3,4a,6-trimethyl-1-(6-methylpyridazin-3-yl)-1,4a-dihydro-4H-benzofuro[3,2-f]indazol-4-one	C ₂₃ H ₂₀ N ₄ O ₅	432.436
39		1-((4R,4aS)-4,5,7-trihydroxy-3,4a,6-trimethyl-1-phenyl-4,4a-dihydro-1H-benzofuro[3,2-f]indazol-8-yl)ethan-1-one	C ₂₄ H ₂₂ N ₂ O ₅	418.449

customizes the docking zone's size depending on the input molecules, and then docks with AutoDock Vina version 1.1.2 [38]. Before docking, a PBD file of the receptor and a mol file containing the ligands were entered into the CB-Dock program. Throughout this method, several top cavities were automatically selected and used for further docking analysis. The ideal binding posture is considered the first conformation, and the associated location is regarded as the best binding site for the query ligand. After examining the binding modalities, interaction with active site residues, and the docking score, the best-docked poses were selected for additional testing compared to the reference compound (Co-crystallized ligand, 11a). The co-crystallized ligand (11a) was selected as reference compound and 11a exhibited high SARS-CoV-2 M^{pro} inhibition activity with the IC₅₀ value of 0.053 ± 0.005 μM. Moreover, this compound showed good PK properties in vivo, and also exhibited low toxicity [34].

MD Simulation and Binding Free-Energy Calculations

The stability of the docked compounds at the M^{pro} enzyme's active site was evaluated by running all-atom MD simulations. While ligand charge calculations were carried out using the bcc method, the topology of M^{pro} and the screened ligands were created using AMBER99SB and GAFF force-fields, respectively [39]. The protein–ligand complexes were solvated in cubical boxes filled with TIP3P water molecules

and then neutralized the system with sufficient Na⁺ and Cl⁻ ions. The distance between the two periodic images was maintained at 2 nm. The systems underwent a 2000-steps steepest descent energy minimization process, followed by a 100-step conjugate gradient energy minimization and subsequently equilibrated for 1 ns each under NVT and NPT ensembles at 310.15 K and 1 bar using modified Berendsen thermostat and Parinello-Rahman barostat, respectively. These equilibrated systems were then subjected to production runs of 100 ns each at the same temperature and pressure. A 2 fs time-step was applied while the frames were updated every 1 ps. Standard GROMACS tools were used for the trajectory analysis, and PyMol was used for viewing the trajectories.

The end-state MMPGSA binding free energy calculations were done using the gmx_MMPBSA v.1.5.2 tool [40]. All the 10,000 frames were taken for binding free energy calculations with the internal and external dielectric constants of 1 and 80, respectively, while iGB model 2 was selected for the analyses. The interaction entropy was calculated for the last 250 frames. The binding free energy is defined by Eq. 1:

$$\Delta G_{\text{gas}} + \Delta G_{\text{solv}} = \Delta G_{\text{total}}, \quad (1)$$

where ΔG_{gas} constitutes the gas phase binding energy contributions, including electrostatic and van der Waals interactions, ΔG_{solv} marks the solvation free energy contribution, and ΔG_{total} represents the total binding free energy.

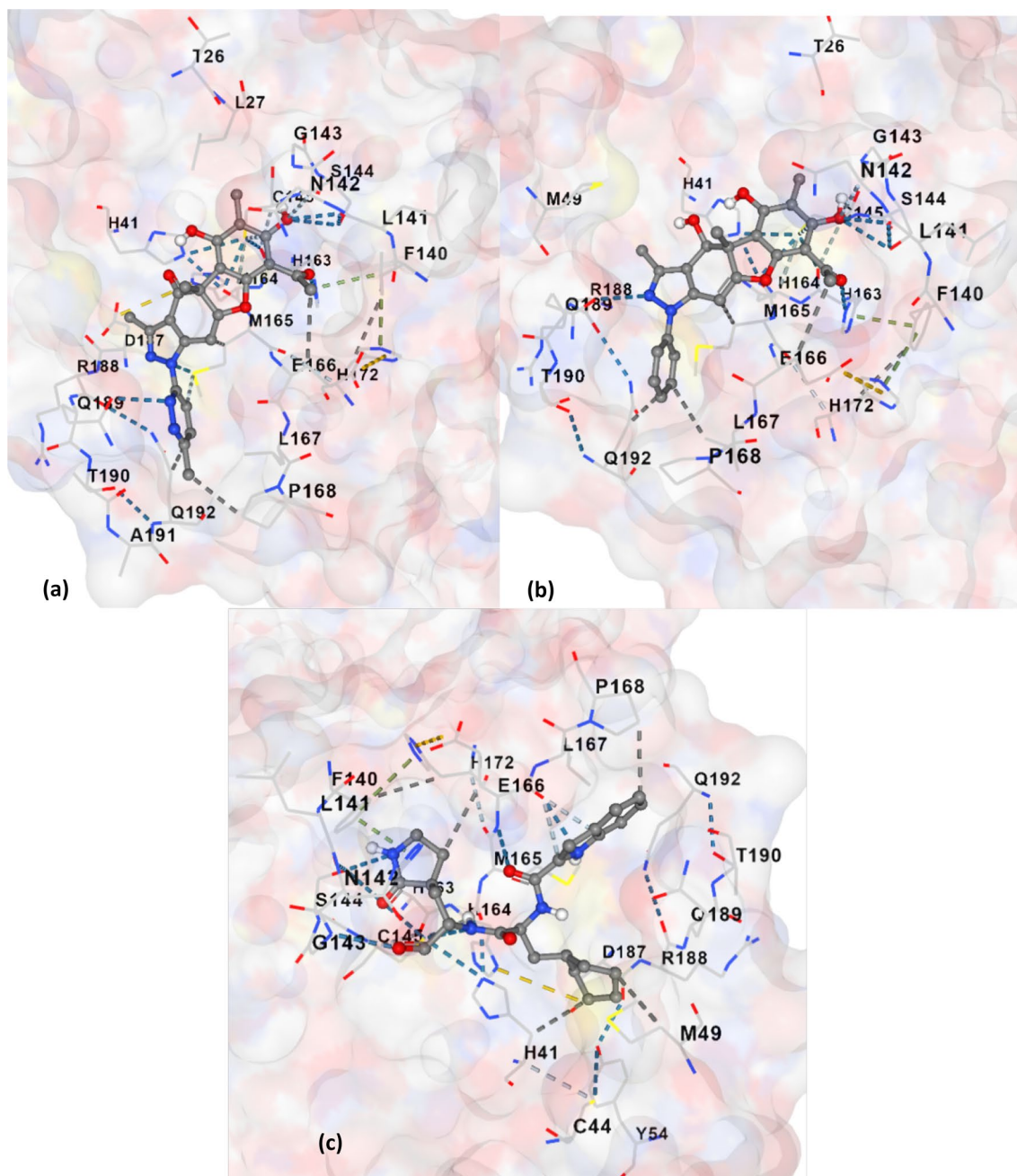


Fig. 1 3D-Interaction diagram of **A** compound 17, **B** compound 39 and **C** Co-crystal ligand 11a with the active site amino acid residues of SARS-CoV-2 main protease

The metadynamics analysis of the trajectory data, including the free energy landscape (FEL), principal component analysis (PCA), cumulative variance, porcupine plot, and secondary structure changes, were estimated using *geo_*measures 0.9 PyMol plugin [41].

Results and Discussion

Drug-Like Properties and ADMET Study

The pharmacokinetic profiles were also calculated for the compounds and the co-crystal ligand (11a). Several predictors, including Lipinski's rule of five and ADMET, were used to characterize these ligands' side effects and potency as drugs. The pkCSM program generates small-compound

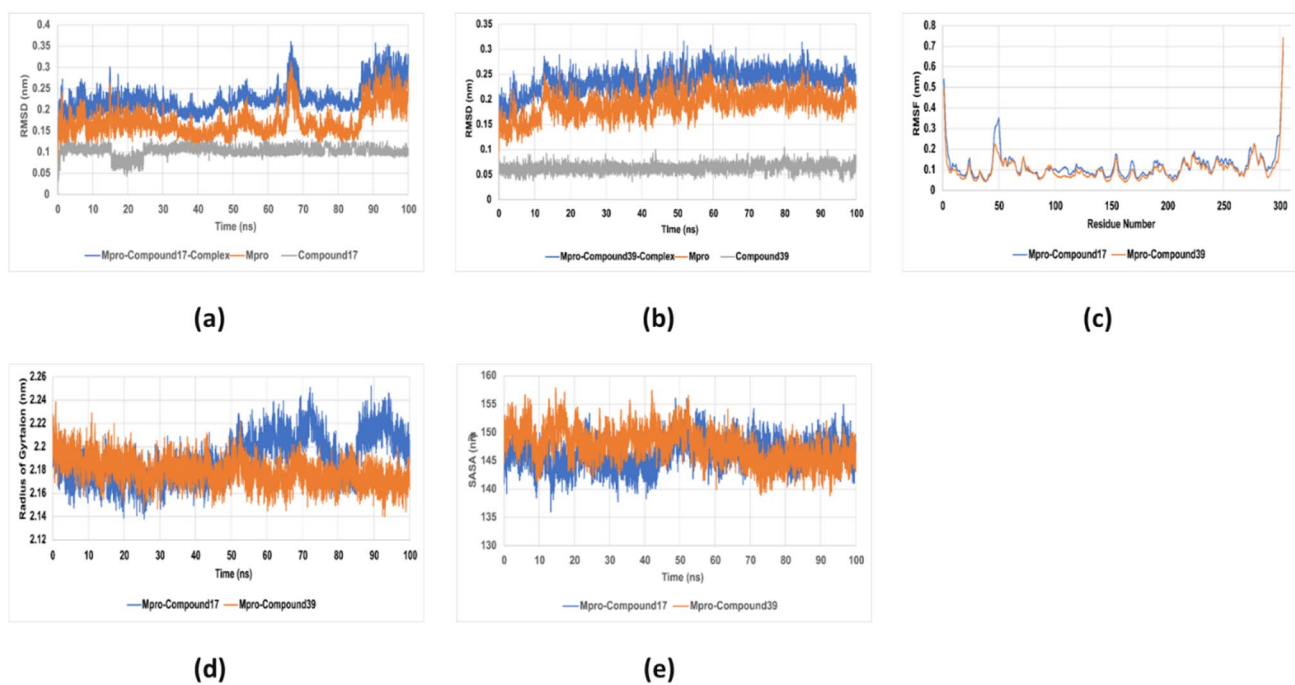


Fig. 2 RMSD plot of individual ligands (a, b) (grey), protein (red) and complex (blue), c RMSF of complex (blue colour-M^{Pro}-compound17 and red colour- M^{Pro}-compound-39), d RoG of complex

(blue colour-M^{Pro}-compound17 and red colour-M^{Pro}-compound-39) and e SASA of complex (blue colour- M^{Pro}-compound17 and red colour- M^{Pro}-compound-39)

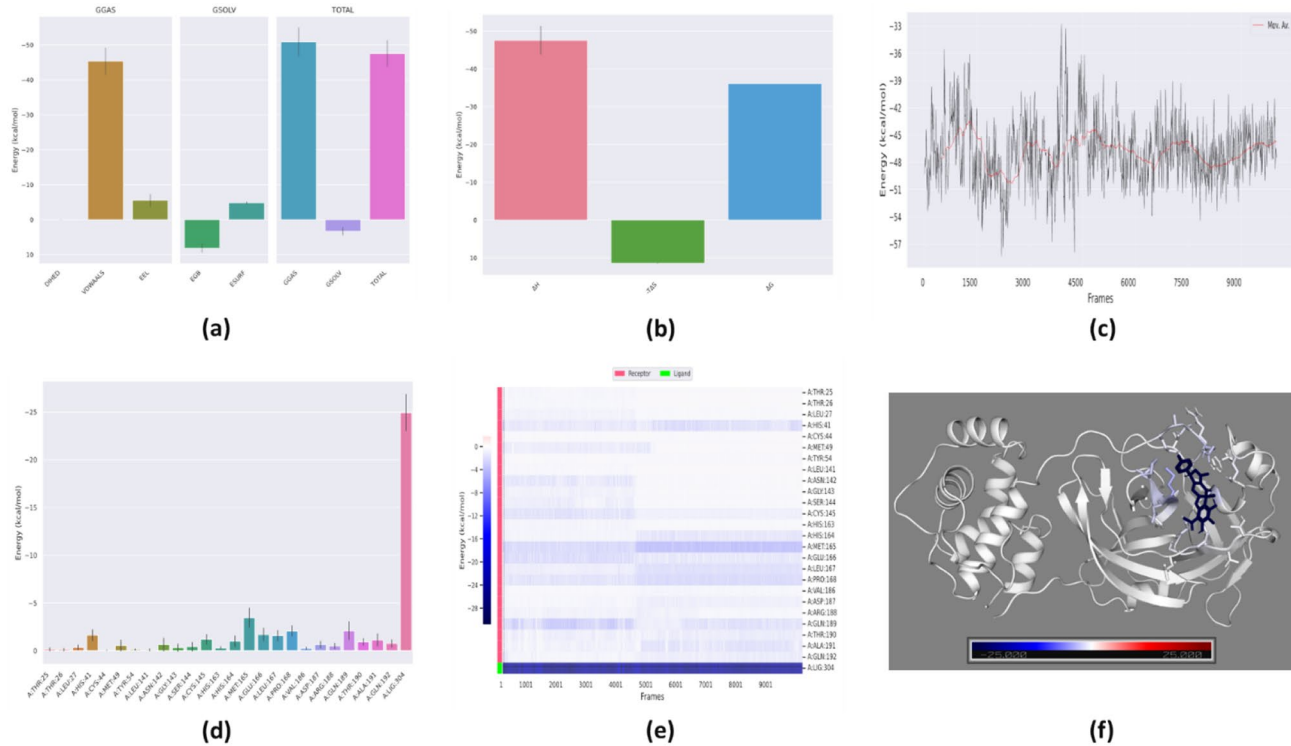
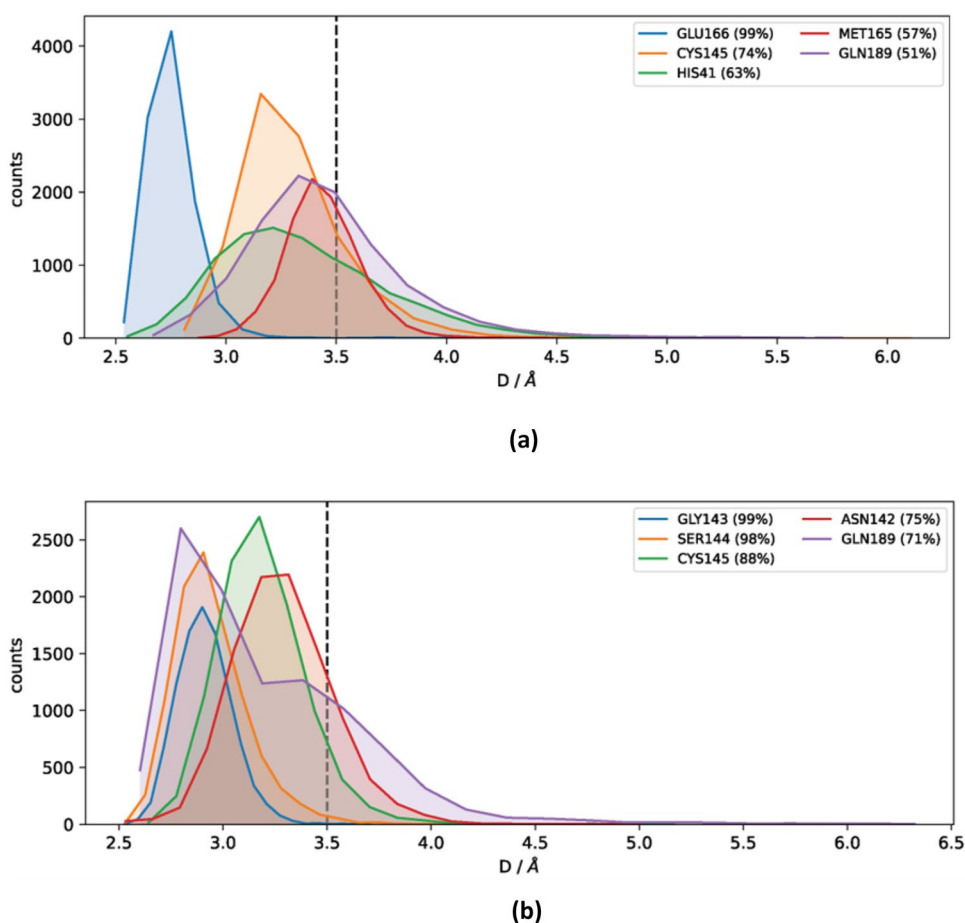


Fig. 3 The binding energy analysis between M^{Pro} and compound- 17. a Enthalpic contributions, b Total binding energy, c Per-frame binding energy values, d Per-residue energy decomposition, e Per-frame

per-residue energy decomposition plot, f 3D representation of energy decomposition of M^{Pro} interacting residues with compound 17

Fig. 5 The number of contacts and their corresponding frequency (51–99%), formed between the ligands and the active site residues of M^{Pro} within 3.5 Å of the ligands. **a** M^{Pro} -compound 17, **b** M^{Pro} -compound-39



protease were obtained during screening. Based on the interaction energy and interacting amino acid residues relative to the reference compound (co-crystal ligand 11a = -8.4 kcal/mol), the two best compounds (17 = -8.9 kcal/mol and 39 = -8.7 kcal/mol) Table 1, which exhibited the similar binding energy and interaction profiles with main protease to that of co-crystal ligand were chosen for future study.

The Usnic acid analogues showed the docked score values on main protease, ranging from -8.4 to -9.7 kcal/mol (Table S3). Figure 1 shows the CB-Dock output data analysis results for selected ligands. Compound 17 was chosen for binding because of its hydrophobic, hydrogen bonding, ionic bonding, and π - π stacking interactions (hydrophobic: Gln192, Pro168, Met165, Phe140, and Glu166; hydrogen bonding: Thr190, Arg188, Met165, Gln189, Cys145, His164, His41, His163, and Leu171; ionic bonds: His164 and His172; π - π stacking: Phe140) (Table S3). Compound-39 had lower binding energy than compound 17, despite having strong hydrophobic, hydrogen bonding, ionic, and π - π stacking interactions (hydrophobic: Gln192, Leu167, Phe140, and Glu166; hydrogen bonding: Thr190, Arg188, Gln189, Met165, His164, Cys145, Leu141, His163, and His41; ionic bond: His172; π - π stacking: Phe140). On

the other hand, compounds 1, 5, 6, 7, 18, 22, and 33 revealed a high number of hydrophobic and hydrogen bond formations with a few similar amino acid residues (Table S3) at the same binding site as Compound 17 and 39. According to the foregoing findings, the ionic and π - π stacking interactions, in addition to hydrogen bonding and hydrophobic interaction, played a crucial part in Compound 17 and 39's high binding affinities compared to other molecules.

MD Simulation

Analysis of Structural Changes and Fluctuations in M^{Pro}

The dynamic behaviors of the screened molecules and their stability at the active site of M^{Pro} were assessed by analyzing their MD trajectories. The root mean square deviation (RMSD) of the individual ligands, protein and complex were calculated and plotted as shown in Fig. 2a and b. Both the systems were well equilibrated within the first 10 ns of the trajectories. In the case of compound 17, the RMSD of the M^{Pro} -compound 17 complex ranged from 0.20 to 0.35 nm, with a similar trend of RMSD for protein from 0.15 to 0.3 nm. The system remained stable from the last 15 ns.

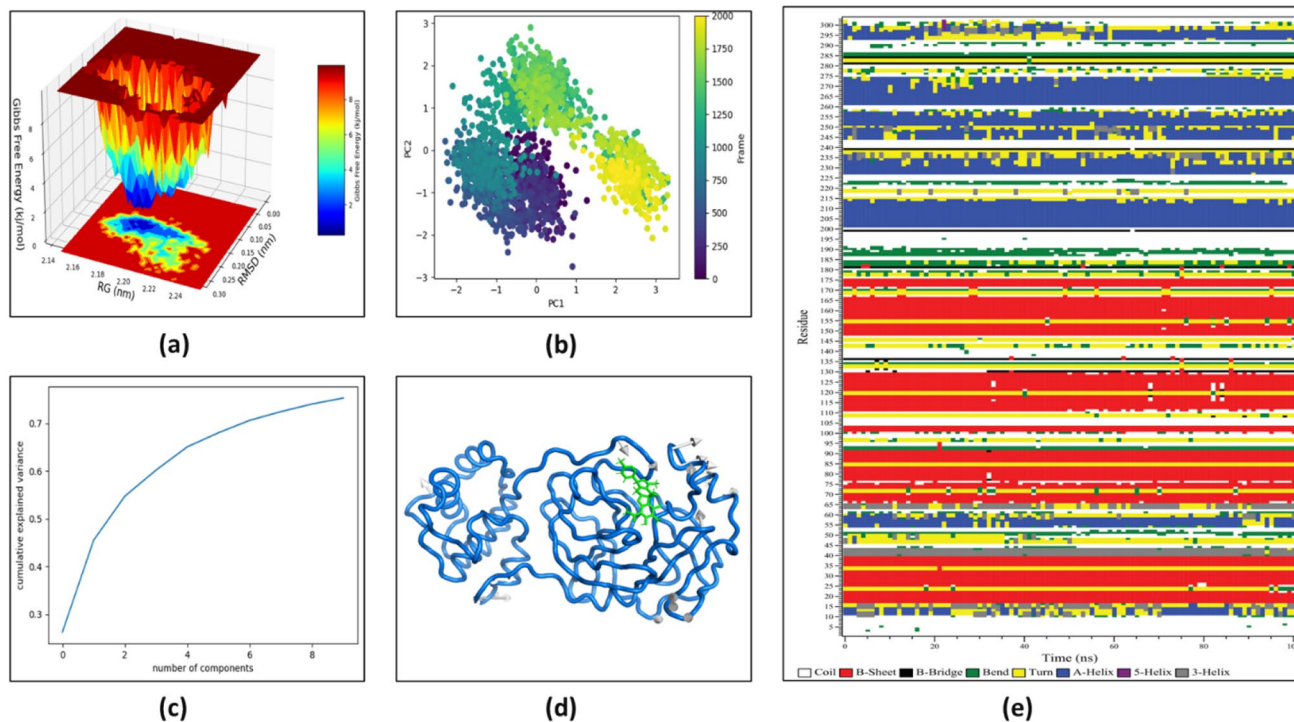


Fig. 6 Metadynamics analysis of M^{Pro} -Compound17 trajectory. **a** Free energy landscape, **b** PCA plot, **c** cumulative variance explained by the first top 10 components, **d** porcupine plot and **e** Changes observed

in the secondary structure around the active site residues of M^{Pro} in complex with compound 17

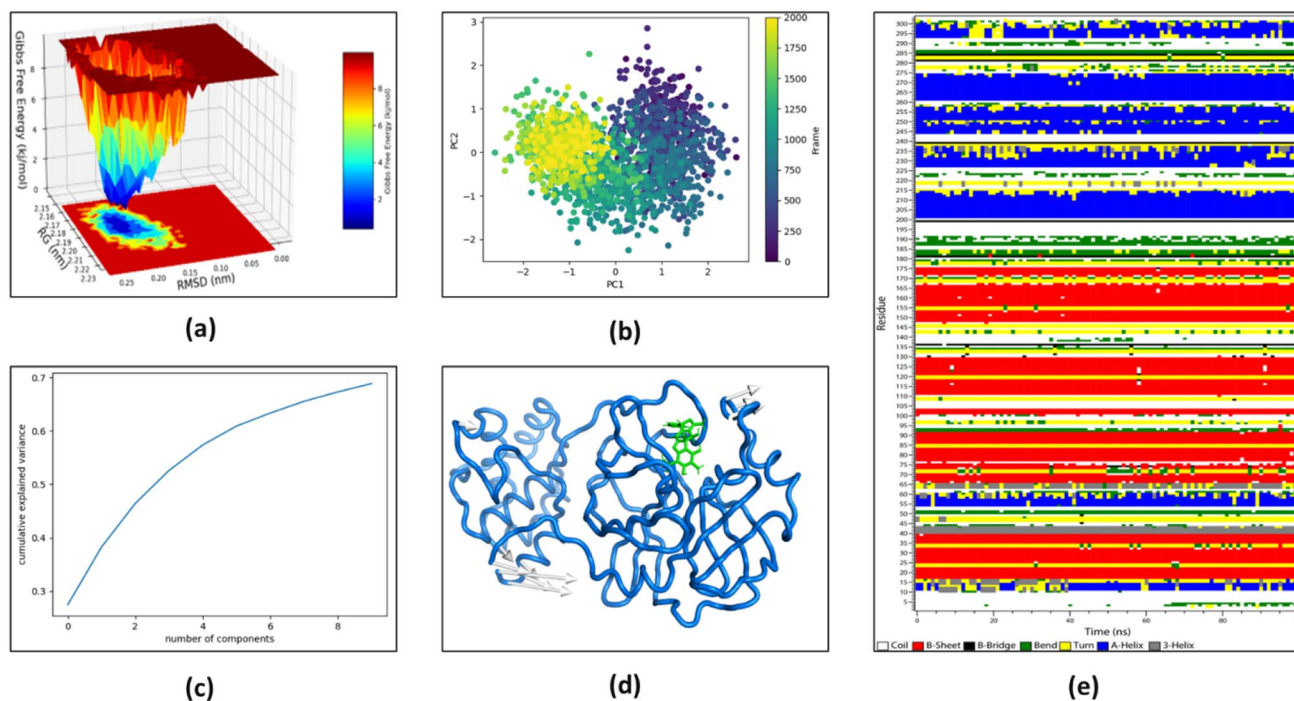


Fig. 7 Metadynamics analysis of M^{Pro} -Compound39 trajectory. **a** Free energy landscape, **b** PCA plot, **c** cumulative variance explained by the first top 10 components, **d** porcupine plot and **e** Changes observed

in the secondary structure around the active site residues of M^{Pro} in complex with compound-39

In comparison, compound 17 showed small fluctuations in RMSD at around 15–24 ns and then remained stable throughout the trajectory with RMSD of 0.11 nm in the case of M^{pro} -compound 39 complex, the RMSD fluctuated from 0.2 to 0.31 nm and remained stable throughout the trajectory. A similar trend of RMSD was seen for M^{pro} . Compound 39 remained steady the entire trajectory with an average RMSD of 0.07 nm. The average fluctuations in the amino acid residues of the protein as a result of ligand binding over the simulation period were assessed by calculating the root mean square fluctuations (RMSF), as evident in Fig. 2c. The RMSF of the residues ranged from 0.05 to 0.75 nm, with the highest fluctuation observed in the terminal residues, which is expected owing to their flexible nature. The minimal fluctuations were observed in the active site residues ranging from 0.05 to 0.12 nm, indicating the stable interactions between the M^{pro} and compounds 17 and 39. The structural changes in M^{pro} were calculated in terms of the radius of gyration of the protein (RoG). Figure 2d shows the RoG of M^{pro} in complex with compound 39 ranged from 2.22 to 2.16 nm and maintained its shape, while M^{pro} in complex with compound 17 showed slight expansion of the structure by the last 50 ns of the trajectory with the RoG values ranging up to 2.25 nm. The solvent accessible surface area (SASA) for the M^{pro} in the presence of ligands remained more or less similar by the end of the simulation for both cases, as shown in Fig. 2e.

Binding Energy Estimations

The end-state relative binding free energies (MMGBSA) between the M^{pro} and compounds 17 and 39 were calculated to assess the stability of these ligands at the active site of M^{pro} . Compound 17 showed a relatively lower binding energy (-36.11 ± 3.76 kcal/mol) with M^{pro} as compared to compound 39, which showed a binding energy of -24.72 ± 3.20 kcal/mol, which indicated a relatively higher affinity of compound 17 towards M^{pro} than compound 39 (Figs. 3a–c and 4a–c) with the major interactions being van der Waals interactions.

The catalytic dyad of M^{pro} consists of the residues His41 and Cys145. For the M^{pro} to be catalytically active, it stays in a homodimeric form, where the residue Glu166 of one protomer interacts with the N-terminal residues of other protomer [3, 46]. Additionally, side chain of Glu166 and His163 along with backbone of Phe140 plays a critical role in peptide substrate recognition and binding. Along with these residues, there are three conserved histidine residues (His163, His162 and His172) that are part of the substrate binding site of M^{pro} . Among these, a mutagenesis study has shown that residues His163 and His172 are critical to maintain the enzymatic activity [47, 48].

In our study, the highest contribution to the binding free energy of M^{pro} with compounds 17 and 39 was made by active site residues Asn142, Gly143, Ser144, His163, His164, Met165, Glu166, Arg188, and Gln189 along with the catalytic dyad residues His41 and Cys145 (Figs. 3d and 4d) which remained stable over the trajectories as shown in Figs. 3e and 4e. These residues also maintained contact with the ligands well under 3.5 Å, with the frequency ranging from 51 to 99%, as shown in Fig. 5. Since, all these residues are critical for dimerization of M^{pro} , peptide substrate recognition, binding and catalysis, hence, binding of compounds 17 and 39 with M^{pro} might interfere with the active homodimer formation, substrate binding and enzymatic catalysis by M^{pro} thereby inhibiting its biological function crucial for SARS-CoV-2 replication.

The Metadynamics Analysis of the Trajectories

The different conformational ensemble states adopted by the protein M^{pro} after binding the compounds 17 and 39 were estimated by plotting the free energy landscapes (Figs. 6a and 7a). A single energy minimum was observed in both cases where the energy minima in the case of compound 17 are more broadened and contain more different ensemble states of the protein compared to FEL of M^{pro} in complex with compound 39 (Figs. 6a and 7a), which is also supported by the PCA analysis and cumulative variance plot where the conformational search spanned by protein in complex with compound 17 is more along both the principal components compared to that in complex with compound 39 (Figs. 6b and 7b) and the cumulative variance explained by the first top 10 components in case of compound 17 is more (78%) as compared to that in case of compound 39 (Figs. 6c and 7c). The slight expansion in the radius of gyration of M^{pro} in complex with compound 17 as compared to complex 39 can also be explained by the outward movement of the alpha-helical fragment over the active site mapped by the residues 46–56 as displayed in the porcupine plot in Figs. 6d and 7d. The changes in the per residue-wise secondary structure of the M^{pro} as a function of screened ligand binding were also assessed. In both cases, no significant changes were observed in the secondary structure around the active site residues (Figs. 6e and 7e).

Conclusions

In conclusion, two novel small compounds that have substantial inhibitory potential against the binding of the M^{pro} , the primary factor responsible for viral infection and replication, were discovered in this work. The newly discovered compounds outperformed the standard (co-crystallized

ligand) molecule. Compared to conventional molecules, they also have greater druggability and favorable pharmacokinetic characteristics. Additionally, MD simulations for 100 ns showed that the interactions between ligands and M^P residues are a crucial component of the residues required for structural stability and functioning. The current in-silico experiments examines compounds' potential (17 and 39) as promising and effective therapeutic medication candidates against SARS-CoV-2.

Supplementary Information The online version contains supplementary material available at <https://doi.org/10.1007/s12033-023-00667-5>.

Acknowledgements The authors would like to thank the Malaysian Cocoa Board for the grant to the Universiti Malaysia Pahang (University Reference Number: RDU 210710) for this project and also thank the HPC facility of IIT Delhi for proving additional software support.

Funding This study was supported by the Lembaga Koko Malaysia (University Reference Number: RDU 210710) to Saiful Nizam Tajuddin.

Data Availability Data can be available upon request.

Declarations

Conflict of interest The authors have no conflict of interest.

References

1. Cavasotto, C. N., & Di Filippo, J. I. (2021). In silico drug repurposing for COVID-19: targeting SARS-CoV-2 proteins through docking and consensus ranking. *Molecular Informatics*, 40(1), 2000115.
2. Hui, D. S., Azhar, E. I., Madani, T. A., Ntoumi, F., Kock, R., Dar, O., & Petersen, E. (2020). The continuing 2019-nCoV epidemic threat of novel coronaviruses to global health—The latest 2019 novel coronavirus outbreak in Wuhan, China. *International Journal of Infectious Diseases*, 91, 264–266.
3. Zhang, L., Lin, D., Sun, X., Curth, U., Drosten, C., Sauerhering, L., & Hilgenfeld, R. (2020). Crystal structure of SARS-CoV-2 main protease provides a basis for design of improved α -ketoamide inhibitors. *Science*, 368(6489), 409–412.
4. Shalayel, M. H., Al-Mazaideh, G. M., Aladaileh, S. H., Al-Swailmi, F. K., & Al-Thiabat, M. G. (2020). Vitamin D is a potential inhibitor of COVID-19: In silico molecular docking to the binding site of SARS-CoV-2 endoribonuclease Nsp15. *Pakistan Journal of Pharmaceutical Sciences*, 33(5), 2179–2186.
5. Kim, Y., Jedrzejczak, R., Maltseva, N. I., Wilamowski, M., Endres, M., Godzik, A., & Joachimiak, A. (2020). Crystal structure of Nsp15 endoribonuclease NendoU from SARS-CoV-2. *Protein Science*, 29(7), 1596–1605.
6. Yadav, R., Chaudhary, J. K., Jain, N., Chaudhary, P. K., Khanra, S., Dhamija, P., & Handu, S. (2021). Role of structural and non-structural proteins and therapeutic targets of SARS-CoV-2 for COVID-19. *Cells*, 10(4), 821.
7. Liu, C., Zhou, Q., Li, Y., Garner, L. V., Watkins, S. P., Carter, L. J., & Albaiu, D. (2020). Research and development on therapeutic agents and vaccines for COVID-19 and related human coronavirus diseases. *ACS Central Science*, 6, 315–331.
8. Joshi, T., Joshi, T., Sharma, P., Mathpal, S., Pundir, H., Bhatt, V., & Chandra, S. (2020). In silico screening of natural compounds against COVID-19 by targeting Mpro and ACE2 using molecular docking. *European Review of Medical Pharmacological Science*, 24(8), 4529–4536.
9. World Health Organization. Naming the coronavirus disease (COVID-19) and the virus that causes it. [https://www.who.int/emergencies/diseases/novel-coronavirus-2019/technical-guidance/naming-the-coronavirus-disease-\(covid-2019\)-and-the-virus-that-causes-it](https://www.who.int/emergencies/diseases/novel-coronavirus-2019/technical-guidance/naming-the-coronavirus-disease-(covid-2019)-and-the-virus-that-causes-it). Accessed on Aug 25, 2022.
10. Majumder, R., & Mandal, M. (2022). Screening of plant-based natural compounds as a potential COVID-19 main protease inhibitor: An in silico docking and molecular dynamics simulation approach. *Journal of Biomolecular Structure and Dynamics*, 40(2), 696–711.
11. <https://www.worldometers.info/coronavirus/>
12. Burki, T. K. (2022). The role of antiviral treatment in the COVID-19 pandemic. *The Lancet Respiratory Medicine*, 10(2), e18.
13. Vardhan, S., & Sahoo, S. K. (2020). In silico ADMET and molecular docking study on searching potential inhibitors from limonoids and triterpenoids for COVID-19. *Computers in Biology and Medicine*, 124, 103936.
14. Ali, A., Sepay, N., Afzal, M., Sepay, N., Alarifi, A., Shahid, M., & Ahmad, M. (2021). Molecular designing, crystal structure determination and in silico screening of copper (II) complexes bearing 8-hydroxyquinoline derivatives as anti-COVID-19. *Bioorganic Chemistry*, 110, 104772.
15. Antonio, A. S., Wiedemann, L. S. M., Galante, E. B. F., Guimarães, A. C., Matharu, A. S., & Veiga-Junior, V. F. (2021). Efficacy and sustainability of natural products in COVID-19 treatment development: Opportunities and challenges in using agro-industrial waste from Citrus and apple. *Heliyon*, 7(8), e07816.
16. Gyselink, I., Janssens, W., Verhamme, P., & Vos, R. (2021). Rationale for azithromycin in COVID-19: An overview of existing evidence. *BMJ Open Respiratory Research*, 8(1), e000806.
17. Cragg, G. M., & Newman, D. J. (2001). Natural product drug discovery in the next millennium. *Pharmaceutical Biology*, 39(sup1), 8–17.
18. Basnet, B. B., Liu, H., Liu, L., & Suleimen, Y. M. (2018). Diversity of anticancer and antimicrobial compounds from lichens and lichen-derived fungi: A systematic review (1985–2017). *Current Organic Chemistry*, 22(25), 2487–2500.
19. Bhattacharyya, S., Deep, P. R., Singh, S., & Nayak, B. (2016). Lichen secondary metabolites and its biological activity. *American Journal of PharmTech Research*, 6(6), 1–7.
20. Fernández-Moriano, C., Gómez-Serranillos, M. P., & Crespo, A. (2016). Antioxidant potential of lichen species and their secondary metabolites: A systematic review. *Pharmaceutical Biology*, 54(1), 1–17.
21. Joshi, T., Sharma, P., Joshi, T., & Chandra, S. (2020). In silico screening of anti-inflammatory compounds from Lichen by targeting cyclooxygenase-2. *Journal of Biomolecular Structure and Dynamics*, 38(12), 3544–3562.
22. Sahoo, B., Dash, S., Parida, S., Sahu, J. K., & Rath, B. (2021). Antimicrobial activity of the lichens *Parmotrema andium* and *Dirinaria applanata*. *Journal of Applied Biology and Biotechnology*, 9(4), 97.
23. Van Cuong, T., & Thoa, N. T. (2018). Bioactive compounds from lichens as promising biomaterial for the treatment of influenza virus: A. *Journal of Scientific Research & Reports*, 18(4), 1–15.
24. Sokolov, D. N., Zarubaev, V. V., Shtro, A. A., Polovinka, M. P., Luzina, O. A., Komarova, N. I., & Kiselev, O. I. (2012). Antiviral activity of (–)- and (+)-usnic acids and their derivatives against influenza virus A (H1N1) 2009. *Bioorganic & Medicinal Chemistry Letters*, 22(23), 7060–7064.

25. Luzina, O. A., & Salakhutdinov, N. F. (2018). Usnic acid and its derivatives for pharmaceutical use: A patent review (2000–2017). *Expert Opinion on Therapeutic Patents*, 28(6), 477–491.
26. Shtro, A. A., Zarubaev, V. V., Luzina, O. A., Sokolov, D. N., Kiselev, O. I., & Salakhutdinov, N. F. (2014). Novel derivatives of usnic acid effectively inhibiting reproduction of influenza A virus. *Bioorganic & Medicinal Chemistry*, 22(24), 6826–6836.
27. Barrera Tomas, M., Tomas Chota, G. E., Sheen Cortavarría, P., Fuentes Bonilla, P., Inocente Camones, M. A., & Contreras, J. S. (2017). Synthesis of acyl-hydrazone from usnic acid and isoniazid and its anti-Myco bacterium tuberculosis activity. *Revista Colombiana de Química*, 46(3), 17–21.
28. Araújo, A. A. S., De Melo, M. G. D., Rabelo, T. K., Nunes, P. S., Santos, S. L., Serafini, M. R., & Gelain, D. P. (2015). Review of the biological properties and toxicity of usnic acid. *Natural Product Research*, 29(23), 2167–2180.
29. Shtro, A. A., Zarubaev, V. V., Luzina, O. A., Sokolov, D. N., & Salakhutdinov, N. F. (2015). Derivatives of usnic acid inhibit broad range of influenza viruses and protect mice from lethal influenza infection. *Antiviral Chemistry and Chemotherapy*, 24(3–4), 92–98.
30. Snetkov, P., Morozkina, S., Olekhovich, R., Vu, T. H. N., Tyanutova, M., & Uspenskaya, M. (2020). Curcumin/usnic acid-loaded electrospun nanofibers based on hyaluronic acid. *Materials*, 13(16), 3476.
31. Takai, M., Uehara, Y., & Beisler, J. A. (1979). Usnic acid derivatives as potential antineoplastic agents. *Journal of Medicinal Chemistry*, 22(11), 1380–1384.
32. Prateeksha, G., Rana, T. S., Asthana, A. K., Singh, B. N., & Barik, S. K. (2021). Screening of cryptogamic secondary metabolites as putative inhibitors of SARS-CoV-2 main protease and ribosomal binding domain of spike glycoprotein by molecular docking and molecular dynamics approaches. *Journal of Molecular Structure*, 1240, 130506.
33. Pires, D. E., Blundell, T. L., & Ascher, D. B. (2015). pkCSM: Predicting small-molecule pharmacokinetic and toxicity properties using graph-based signatures. *Journal of Medicinal Chemistry*, 58(9), 4066–4072.
34. Dai, W., Zhang, B., Jiang, X. M., Su, H., Li, J., Zhao, Y., & Liu, H. (2020). Structure-based design of antiviral drug candidates targeting the SARS-CoV-2 main protease. *Science*, 368(6497), 1331–1335.
35. Amin, S., Banerjee, S., Singh, S., Qureshi, I. A., Gayen, S., & Jha, T. (2021). First structure–activity relationship analysis of SARS-CoV-2 virus main protease (Mpro) inhibitors: An endeavor on COVID-19 drug discovery. *Molecular Diversity*, 25(3), 1827–1838.
36. Mishra, P. M., & Nandi, C. K. (2021). Structural Decoding of a Small Molecular Inhibitor on the Binding of SARS-CoV-2 to the ACE 2 Receptor. *The Journal of Physical Chemistry B*, 125(30), 8395–8405.
37. Padhi, A. K., Seal, A., Khan, J. M., Ahamed, M., & Tripathi, T. (2021). Unraveling the mechanism of arbidol binding and inhibition of SARS-CoV-2: Insights from atomistic simulations. *European Journal of Pharmacology*, 894, 173836.
38. Liu, Y., Grimm, M., Dai, W. T., Hou, M. C., Xiao, Z. X., & Cao, Y. (2020). CB-Dock: A web server for cavity detection-guided protein–ligand blind docking. *Acta Pharmacologica Sinica*, 41(1), 138–144.
39. Huggins, D. J. (2022). Comparing the performance of different AMBER protein forcefields, partial charge assignments, and water models for absolute binding free energy calculations. *Journal of Chemical Theory and Computation*, 18(4), 2616–2630.
40. Bhardwaj, V., Singh, R., Singh, P., Purohit, R., & Kumar, S. (2020). Elimination of bitter-off taste of stevioside through structure modification and computational interventions. *Journal of Theoretical Biology*, 486, 110094.
41. Kagami, L. P., das Neves, G. M., Timmers, L. F. S. M., Caceres, R. A., & Eifler-Lima, V. L. (2020). Geo-Measures: A PyMOL plugin for protein structure ensembles analysis. *Computational Biology and Chemistry*, 87, 107322.
42. Bhupinder Singh, K. (2007). Practitioners section-Cytochrome P450 enzyme isoforms and their therapeutic implications: An update. *Indian Journal of Medical Sciences*, 61(2), 102–116.
43. Gianulis, E. C., & Trudeau, M. C. (2011). Rescue of aberrant gating by a genetically encoded PAS (Per-Arnt-Sim) domain in several long QT syndrome mutant human ether-a-go-go-related gene potassium channels. *Journal of Biological Chemistry*, 286(25), 22160–22169.
44. Aromolaran, A. S., Srivastava, U., Alí, A., Chahine, M., Lazaro, D., El-Sherif, N., & Boutjdir, M. (2018). Interleukin-6 inhibition of hERG underlies risk for acquired long QT in cardiac and systemic inflammation. *PLoS ONE*, 13(12), e0208321.
45. Nattel, S., & Carlsson, L. (2006). Innovative approaches to antiarrhythmic drug therapy. *Nature Reviews Drug Discovery*, 5(12), 1034–1049.
46. Bhardwaj, V. K., Singh, R., Sharma, J., Rajendran, V., Purohit, R., & Kumar, S. (2020). Identification of bioactive molecules from Tea plant as SARS-CoV-2 main protease inhibitors. *Journal of Biomolecular Structure and Dynamics*, 39(10), 3449–3458.
47. Al Adem, K., Ferreira, J. C., Fadl, S., & Rabeh, W. M. (2022). pH profiles of 3-chymotrypsin-like protease (3CLpro) from SARS-CoV-2 elucidate its catalytic mechanism and a histidine residue critical for activity. *Journal of Biological Chemistry*, 299, 102790.
48. Weng, Y. L., Naik, S. R., Dingelstad, N., Lugo, M. R., Kalyaanamoorthy, S., & Ganesan, A. (2021). Molecular dynamics and in silico mutagenesis on the reversible inhibitor-bound SARS-CoV-2 main protease complexes reveal the role of lateral pocket in enhancing the ligand affinity. *Scientific Reports*, 11(1), 1–22.

Publisher's Note Springer Nature remains neutral with regard to jurisdictional claims in published maps and institutional affiliations.

Springer Nature or its licensor (e.g. a society or other partner) holds exclusive rights to this article under a publishing agreement with the author(s) or other rightsholder(s); author self-archiving of the accepted manuscript version of this article is solely governed by the terms of such publishing agreement and applicable law.